Journal of Alloys and Compounds 816 (2020) 152584

Contents lists available at ScienceDirect

Journal of Alloys and Compounds

journal homepage: http://www.elsevier.com/locate/jalcom

Microstructure and mechanical response of TiB_2/Al–Zn–Mg–Cu composites with more addition of Zn

Q. Yang [a], Y. Shen [b], J. Liu [a], L. Wang [a], Z. Chen [a, *], M.L. Wang [c], S.Y. Zhong [c, **], Y. Wu [c], H.W. Wang [a]

[a] State Key Laboratory of Metal Matrix Composites, Shanghai Jiao Tong University, Shanghai, 200240, PR China
[b] EDF R&D, Département Matériaux et Mécanique des Composants, Avenue des Renardieres - Écuelles, F-77250, Moret sur Loing, France
[c] School of Materials Science and Engineering, Shanghai Jiao Tong University, Shanghai, 200240, PR China

ARTICLE INFO

Article history:
Received 21 June 2019
Received in revised form
1 September 2019
Accepted 5 October 2019
Available online 7 October 2019

Keywords:
Precipitation kinetics
Al–Zn–Mg–Cu
Composites
Powder metallurgy

ABSTRACT

In the present work, the in-situ TiB_2/Al–Zn–Mg–Cu composites with different content of Zn element were fabricated by powder metallurgy. The interphases composed of solute elements are preferentially nucleated at the facets of the TiB_2 particles during heating and the clusters in local region hinder the dissolution of the interphases into the matrix. Additionally, the phenomena of accelerated age-hardness response and reduced work hardening rate with increasing Zn content are found experimentally for TiB_2/Al–Zn–Mg–Cu composites fabricated by powder metallurgy. A physically-based numerical model is developed to predict the precipitation kinetics and hardness as a function of aging time. The advanced reach to peak hardness results from accelerated nucleate rate and growth rate due to more addition of solute content. The influence of Zn content on the work hardening rate is discussed based on the state-parameters including solute content in the matrix, precipitate size and volume fraction. The effect of TiB_2 particles on the parameters of the size class model is discussed qualitatively based on the experimental observations.

1. Introduction

For precipitates containing alloys such as for Al–Zn–Mg alloys [1,2], Al–Cu–Mg alloys [3,4], Al–Mg–Si alloys [5,6] and their composites, the physical characters, volume fraction and size of precipitates have a significant effect on the mechanical properties. Both aging treatment and solution treatment involved with complex diffusion process of solute elements and chemical stability of second phases are crucial to microstructure evolution.

The studies on the solution process and precipitation kinetics mainly focus on the solute-rich alloys [7–12]. In general, the isothermal/non-isothermal dissolution of the coarse interphases including T (AlZnMgCu) phases and S (Al2CuMg) phases are characterized by scanning electron microscope (SEM) and X-ray diffraction (XRD) [7–9]. Likewise, the precipitation kinetics as a function of aging time has been studied experimentally by different types of equipment [10–12] and theoretically by different models [13–16]. However, the studies on the solution treatment and aging treatment for the composites reinforced by the particles are rare, especially on solution treatment. Additionally, these studies mainly focus on the particles with micron-scale usually with tens microns. In these studies, the accelerated aging hardening response is observed for the composites with particles in tens of microns size, which is attributed to the formation of geometrically necessary dislocations (GNDs) and matrix plastic deformation zones due to different coefficient of thermal expansion [17–20]. The effect of the nanoparticles on the aging treatment is rarely studied.

Furthermore, the studies on the particles on the solution treatment are limited to the composites fabricated by castings, and there are rare studies on the effect of particles on the interphase evolution in the composites fabricated by powder metallurgy. During casting, the coarse interphases such as T (AlZnMgCu) phases and S (Al_2CuMg) phases incorporated with particles clusters along the grain boundaries are formed [21,22]. The TiB_2 particles acting as shielding shells prevent the dissolution process due to the reduced contact area between interphases and Al matrix [22]. Therefore, coarse interphases still exist even after solution treatment.

* Corresponding author.
** Corresponding author.
E-mail addresses: zhe.chen@sjtu.edu.cn (Z. Chen), shengyi.zhong@sjtu.edu.cn (S.Y. Zhong).

https://doi.org/10.1016/j.jallcom.2019.152584
0925-8388/

However, there is no formation of coarse interphases in the composite powders with nanoparticles due to the large cooling rate in the process of gas atomization, and the particles are no longer aggregated along the grain boundaries [23]. However, the fine interphases will form from the saturated master alloy and vary from a few hundred nanometers in the very small particles to a few microns when the powders are subjected to sintering [24]. The interaction of the diffused solute elements and ceramic particles is rarely investigated.

Additionally, one of the great advantages of powder metallurgy and spray deposition is to avoid the solute macrosegregation, microstructure coarsening and cracking in the Al–Zn–Mg–Cu castings with a practical limit content of 8 wt.% Zn [25]. It is well acknowledged that the mechanical properties of the composites depend on both ceramic particles and metal matrix. As for Al–Zn–Mg–Cu matrix composites, the properties of metal matrix are substantially affected by solute elements such as Zn content. In our previous work, Wang et al. [26] have studied the microstructure and mechanical properties of extruded TiB_2/Al–Zn–Mg–Cu composites with Zn content range from 6.9 wt % to 12 wt %, and concluded that the yield strength increased from 597 MPa to 707 MPa and the TiB_2 particles are more uniformly dispersed within grains due to reduced interfacial energy. Nie et al. [27] have found that the metastable GP zones or η′ phases transformed into stable η phases and the strength increased with increasing Zn content from 9 wt % to 11 wt % in Al–Zn–Mg–Cu alloys. With increasing Mg content from 1 wt % to 2 wt % in Al-8.0Zn-xMg-1.6Cu alloys, the driving force of η phases increases and the maximum hardness values increases [28]. These studies are mainly based on the experimental observations, and lack of precipitation kinetics analysis. The effect of solute elements on the aging hardness response is rarely studied. The optimum heat treatment parameters should vary with different solute elements for age-hardening alloys.

The present work was undertaken to investigate the microstructure evolution of the TiB_2/Al–Zn–Mg–Cu composites fabricated by powder metallurgy, especially focus on the microstructure after extrusion and aging treatment. The microstructure concerning the interaction of the solute elements and TiB_2 particles was detailed studied. Additionally, the effects of the Zn content on the microstructure especially after aging treatment and precipitation kinetics were studied experimentally and theoretically.

2. Experimental procedure

The measured compositions of three TiB_2/Al–Zn–Mg–Cu composites with different Zn content are listed in Table 1. The Zn content in the widely used 7050 alloys ranges from 5.7 wt % to 6.7 wt %. The maximum content of Zn elements in Al–Zn–Mg–Cu alloys is 11.5 wt % in 7034 alloys. In the present work, the designed Zn content is range from 6.7 wt % to 11.5 wt %. The Zn content has a little loss during the process of remelting and gas atomization. At first, the TiB_2/Al–Zn–Mg–Cu composites ingots were prepared by casting [29]. The ingots were then put in the crucible and superheated to about 780 °C holding for 30 min. The ingots were completely melted. Then the superheated melt was delivered to the atomizer and the melt would break down into droplets under the impact of rapid moving N_2. The droplets would be cooled and solidified due to extensive heat transfer between droplets and N_2 [30]. The cooled and solidified powders were then collected. More details about the fabrication of nano-TiB_2 particles decorated aluminum alloy powders can be found in ref. [31]. The composite powders were then placed in a graphite die with a 40 mm inner diameter and 80 mm in height, and then directly subjected to spark plasma sintering (SPS) on an FCT H-HP D 25 system. The sintering experiments were carried out at the temperature of 480 °C and under uniaxial loading of 50 MPa for 5 min. The heating rate was about 50 °C/min, the standard 12:2 pulse sequence was adopted. Then the compacts were subjected to hot extrusion into bars at the temperature of 450 °C with an extrusion rate of 0.8 mm/s and extrusion ratio of 16. The slow heating rate leads to the formation of interphases such as T (AlZnMgCu) phases. The solution treatment of as-extruded composites was conducted at the temperature of 475 °C for 1 h and then water quenched to room temperature. Then the composites were immediately aged at 120 °C for different hours.

Table 1
Compositions of the experimental composites.

Samples	Al (wt. %)	Zn (wt. %)	Mg (wt. %)	Cu (wt. %)	Ti (wt. %)	B (wt. %)
A	Bal.	6.28	2.13	2.42	4.79	2.14
B	Bal.	8.32	2.18	2.38	4.70	2.10
C	Bal.	10.93	2.29	1.23	4.62	2.06

The microstructure of the as-extruded and as-aged specimens was characterized by TESCAN MAIA3 scanning electron microscope (SEM) and equipped BRUKER e-FlashHR electron backscatter diffraction (EBSD) detector. The TEM specimens were prepared by cutting a disc in 1 mm thickness from the aged bars perpendicular to the extrusion direction. Then the discs were ground carefully to a thickness of 60 μm and twin-jet electropolished in a mixture of 70 ml nitric and 210 ml methanol at the temperature of −30 °C at a working voltage of 20 V. The TEM experiments were carried out on Talos F200X equipped with STEM detector operated at 200 kV.

The tensile tests were conducted on a Zwick/Roell machine at a strain rate of 10^{-4} s^{-1} in the extrusion direction. The size of specimens for tensile tests was 5 mm in diameter and 25 mm in gauge.

3. Results

3.1. Microstructures

The microstructures of the as-extruded samples A, B, and C are shown in Fig. 1a ~ c in backscattered electron (BSE) mode, respectively. The phases in bright contrast are the formed interphases and the particles in grey contrast are the introduced TiB_2 particles. The active solute elements tend to form interphases under the process of heating until the desired extrusion temperature. The polythermal section of Al–Zn–Mg–Cu–Zr phase diagram for Zn = 8 wt %, Cu = 2 wt %, Zr = 0.3 wt %, Mg from 0 to 8 wt % shows that Al_2CuMg (S) phase and AlZnMgCu (T) phase should exist when heating to 450 °C [32]. DSC patterns show that the η phase would be dissolved into matrix above 200 °C [27] and the S phases would form at the temperature range of 250–400 °C [33]. Therefore, the main interphases are the mixture of S phases and T phases. The T phases composed of Al, Zn, Mg, Cu elements are preferentially formed at the facet of TiB_2 particles as shown by the red rectangular marks in Fig. 2a of composite B. And the chemical composition of T phases nucleated at the different facets of the TiB_2 particles are different based on point EDS as shown in Fig. 2b. Fig. 2c shows the EDS line scanning of Ti, Zn, Mg, Cu elements along the red line in Fig. 2b. Fig. 2d is the STEM micrograph, which also shows the nucleation of the T phase on the TiB_2 particles. The EDS mappings are provided. The structure of T phases is body-centered. The interface between the Al matrix and T phases is provided by HRTEM as shown in Fig. 2e. The view is along with the $[0\ 0\ 1]_{Al}$ direction. The inset is the FFT of the red marked area in Fig. 2e. The orientation of T phases and Al matrix is summarized as follows:

$[0\ 0\ 1]_{Al}//[1\ 1\ 3]_T$, $(-2\ 2\ 0)_{Al}//(3\ 3\ 0)_T$

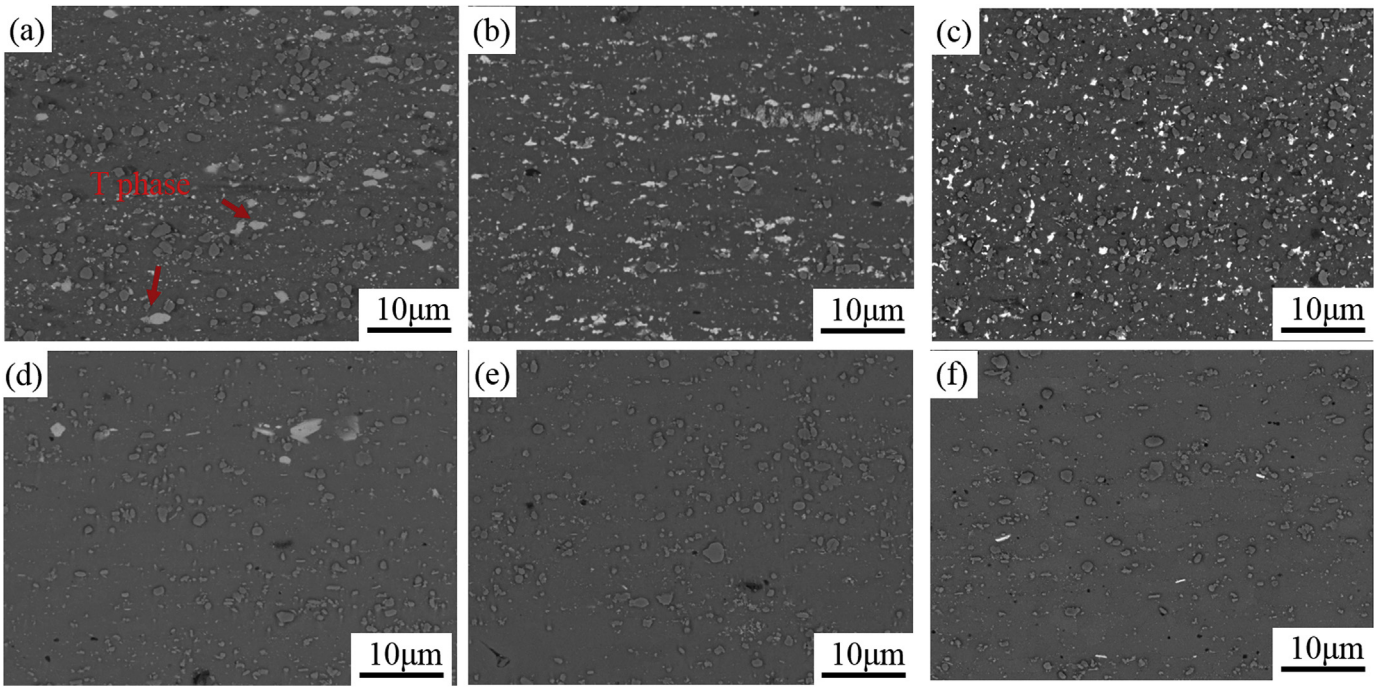

Fig. 1. The microstructure of the as-extruded (a) composites A; (b) composites B; (c) composites C, respectively; the microstructure of the as-aged (d) composites A; (e) composites B; (f) composites C respectively.

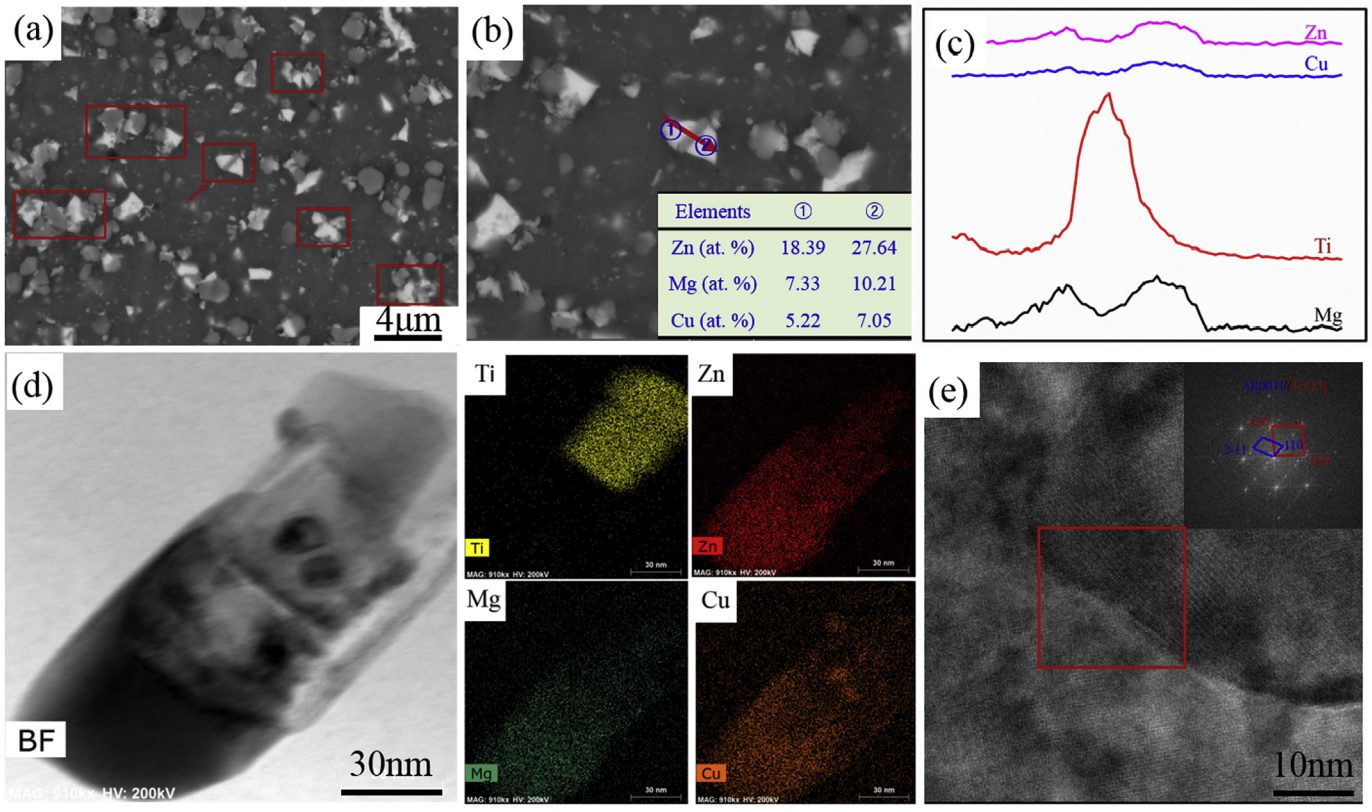

Fig. 2. (a) The microstructure of the as-extruded sample B, the red rectangular marks show the preferential nucleation of interphases at the facet of the TiB_2 particles; (b) the larger magnification of the red arrow in the (a), the inset is the point EDS at the location 1 and 2; (c) the EDS line scanning along the red arrow in Fig. 2(b); (d) the STEM micrograph of the as-extruded sample B, the EDS mappings of Zn, Mg, Cu and Ti elements are provided; (e) the HRTEM image of the interface between the interphase and Al matrix, the inset is the FFT. (For interpretation of the references to colour in this figure legend, the reader is referred to the Web version of this article.)

The content of solute elements is supposed to affect the volume fraction of the formed interphases. In the present work, the relative fraction of the formed interphases with different content of Zn elements is qualitatively analyzed by the relative intensity of XRD peaks as shown in Fig. 3. Fig. 3a and b shows the XRD patterns of as-extruded and as-aged composites respectively. The diffraction peaks located between peaks of (1 1 1)Al and (2 0 0)Al are supposed to arise from the mixture of T phases and S phases. The higher of Zn elements content, the higher peak intensity of interphases, indicating the higher fraction of interphases (T and S) formed during hot extrusion.

The microstructures of the aged samples A, B, C are given in Fig. 1d–f. The submicron TiB_2 particles are uniformly distributed in the aluminum alloy matrix. There are no TiB_2 clusters observed. And the formed interphases composed of solute elements are almost dissolved into matrix after solution. The absence of XRD peaks of interphases as shown in Fig. 3b also collaborates the dissolution of interphases. However, there are still residual interphases containing Cu elements in the matrix due to the slower diffusion coefficient of Cu elements [34].

Fig. 4 shows the local bright-field TEM microstructure of the as-aged composite B. There are some residual interphases which are surrounded by local TiB_2 particles in Fig. 4a. The EDS mappings of Ti elements and solute elements are given. The local particles clusters prevent the dissolution of the interphases during solution treatment. There are also interphases observed neighboring to single TiB_2 particle at the grain boundary in Fig. 4b. The EDS mappings of Ti elements and solute elements are also given. Therefore, although most of the interphases are dissolved into matrix after solution treatment, the local TiB_2 particles clusters and grain boundaries influence the dissolution process of the interphases.

Fig. 5a–c give the bright-field TEM images for the samples A, B and C aged at 120 °C for 24 h. Fig. 5d–f shows the high-resolution transmission electron micrographs (HRTEM) of the three samples correspondingly in the <112>Al orientation. As it is observed, there are a large amount of plate-like precipitates formed after aged for 24 h. The precipitates are preferentially nucleated at the Al (111) planes due to small lattice misfit. The solute atoms are easier to adhere to Al (111) planes rather than along the <111> direction. Therefore, the disk surface of the plate-like precipitates grows at a rapid rate. Fig. 5g shows the schematic illustration of plate-like precipitates lying on the {1 1 1}Al planes in the Al matrix. There are several equivalent {111} planes in one lattice. When viewed along the Al <112> direction, the precipitates exhibit rectangular and elliptical shape in the projection plane as HRTEM images observed. It has been reported [10,27,34,35] that there are several types of precipitates in Al–Zn–Mg–Cu alloy including coherent GP zones, semi-coherent η′ phases and η phases. As it is shown, the number density of the precipitates increases with more addition of Zn content. Fig. 6 shows the selected area electron diffraction (SAED) of sample A in <112> direction and sample C in <001> direction. Weak diffraction spots at 1/3 {220} Al and 2/3 {220} Al viewed along in <0 0 1> direction and weak streaks at 1/3 {220} Al and 2/3 {220} Al viewed along in <112> direction come from η′ phases. Weak spots at 1/3 {311} Al and 2/3 {311}Al in <112> direction and at {1, (2n+1)/4, 0} positions in [001] direction come from GPI zones. Weak diffraction spots in 1/2 {131} positions viewed along <112> direction comes from GPII zones. According to the results of HRTEM and SAED, the main precipitates are the semi-coherent η′ phases and GP zones, and the stable η phases are not formed even with highest Zn content in the present work. However, it was reported [27] that the precipitates in Al–Zn–Mg evolved from metastable η′ phases to stable η phases when the Zn content increased from 9 wt % to 11 wt %. The average radius of the precipitates in samples A, B, C aged for 24 h measured by HRTEM is 3.12, 2.79 and 2.6 nm respectively. The precipitate radius decreases little with increasing Zn content.

Fig. 7 shows the bright-field TEM images obtained from the vicinity of grain boundaries in the three samples with different Zn content addition. In general, the width of precipitate free zones (PFZs) is narrow. And with increasing Zn content from 6.28 wt % to 10.93 wt %, the width of PFZs decreases from 31 nm to 16 nm. The PFZs are also observed around the TiB_2 particles as shown in Fig. 8. The larger precipitates around the particles which has been reported in ref. [17] are not found. Most studies focused on the PFZs in the vicinity of the grain boundaries. The existence of the PFZs is generally explained in terms of vacancy depletion or solute depletion [36,37]. The precipitation process involves the diffusion of solute elements which requires excessive vacancy concentration. The vacancy depletion mechanism considers the fact that the grain boundaries are the effective vacancy sink sites [38,39]. In the case of solute depletion mechanism, it is found that the occurrence of PFZs usually accompanies with the formation of coarse grain boundary precipitates (GBPs). The formation of these coarse and stable GBPs gives rise to depletion of solute elements near grain boundaries [40,41]. Therefore, the metastable precipitates cannot form near the grain boundaries due to lowered solute concentration. It is obvious that the width of PFZs decreases with increasing Zn content due to more supersaturated Zn content in terms of solute depletion mechanism. The occurrence of PFZs around second phases is less studied. Sanders et al. [42] observed a PFZ around Al_6Mn intermetallic compound in Al–Li–Mn alloy. The formation mechanism is not discussed. Song et al. [43] observed a PFZ around primary carbides in nickel base alloy 725. The width of the PFZs is controlled by the elastic stress field simulated by finite element analysis. The similar result can be found that narrower PFZs occurred at the

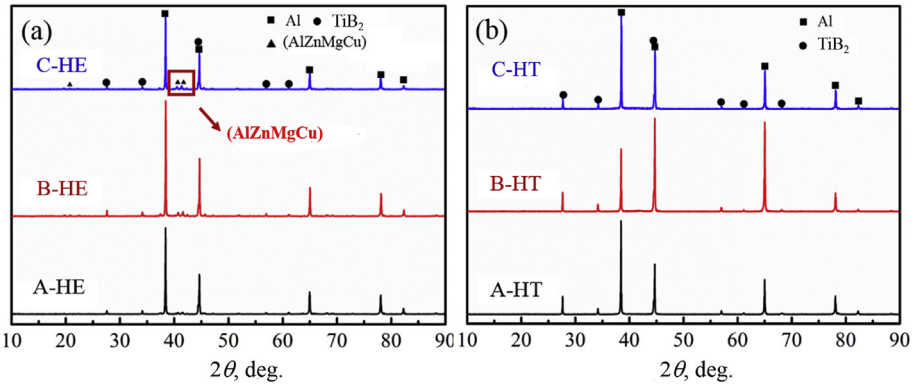

Fig. 3. The XRD patterns of (a) the as-extruded composites; (b) the as-aged composites.

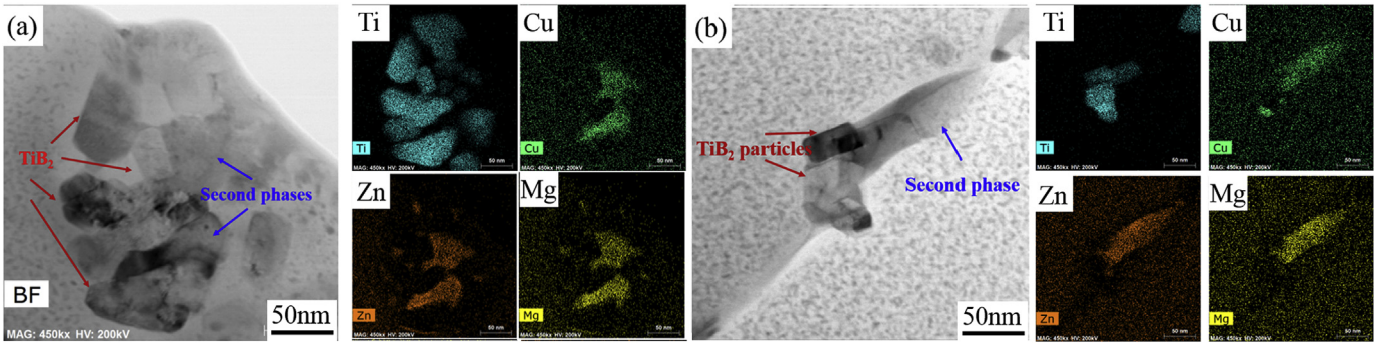

Fig. 4. The bright-field TEM micrographs of the as-aged composites B showing the undissolved interphases (AlZnMgCu phase) around TiB_2 particles clusters.

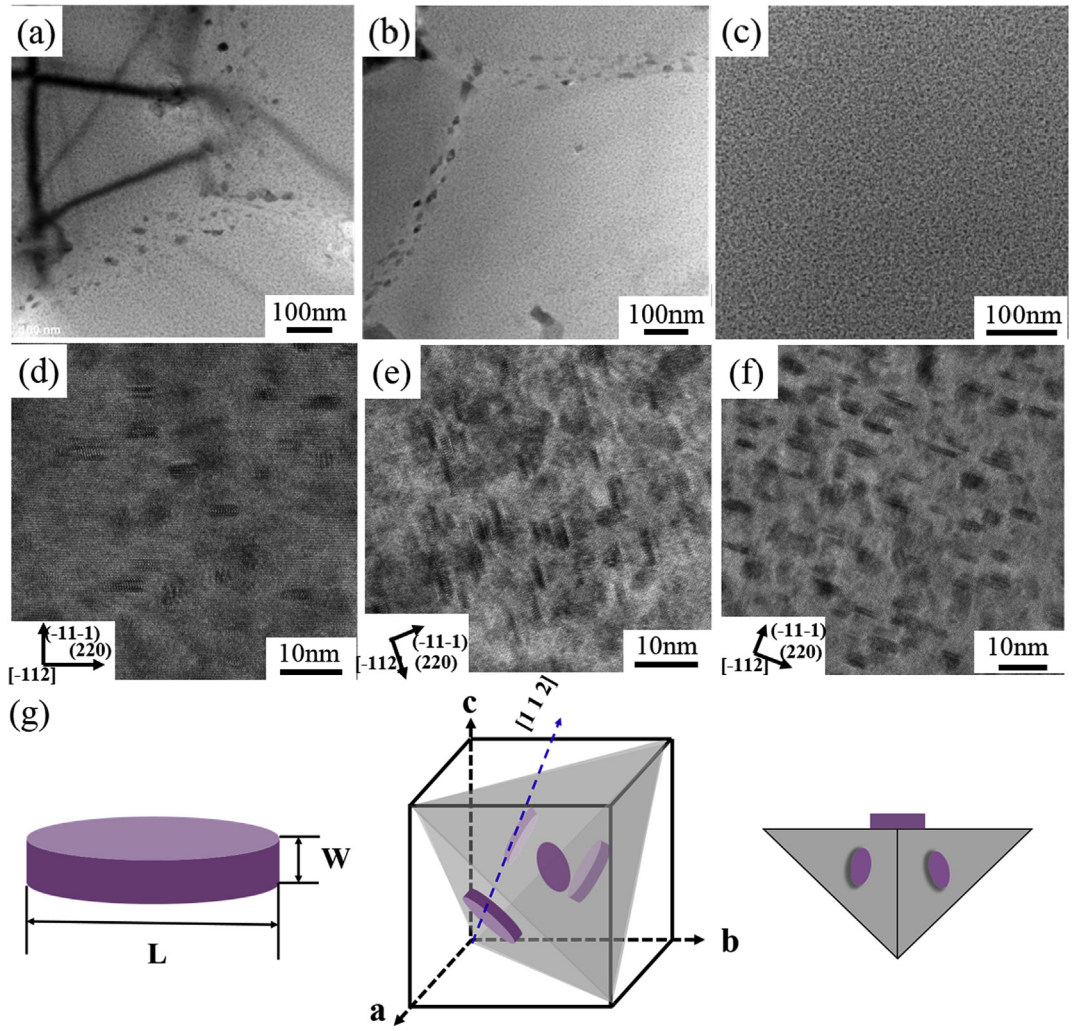

Fig. 5. The bright-field TEM micrographs of the (a) composite A; (b) composites B; (c) composites C aged for 24 h respectively; the HRTEM images of the as-aged (d) composites A; (e) composites B; (f) composites C along the <112>Al direction; (g) The schematic illustration of plate-like precipitates lying on the {1 1 1}Al planes in the Al matrix.

corner of the particles and wider PFZ occurred at the facet of the particles as shown in Fig. 8b. It is resulted from enhanced precipitation process by tensile stress and suppressed precipitation process by compressive stress.

3.2. Mechanical properties

The aging hardening curves at 120 °C of the investigated composite are shown in Fig. 9. All the composites show a rapid aging hardening response. The hardness of the as-extruded composites is nearly identical about 100 HV. After solution treatment, the hardness of the three samples increases to 148 HV, 160 HV, 169 HV respectively. The higher hardness of composites with more Zn elements addition results from solution strengthening effect. The contribution of solution strengthening is proportional to the square root of the solute content in the matrix [2]. After aging for 6 h for

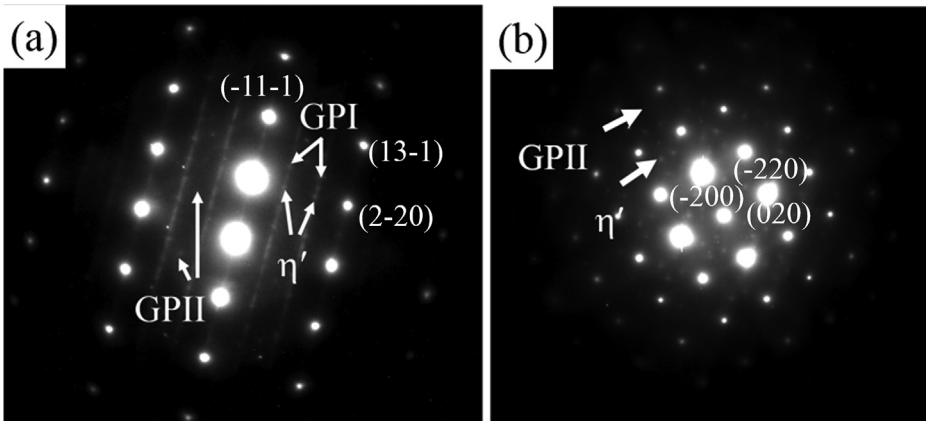

Fig. 6. The selected area electron diffraction (SAED) patterns of (a) composite A aged for 24 h along <112>Al; (b) composites C aged for 24 h along <001>Al.

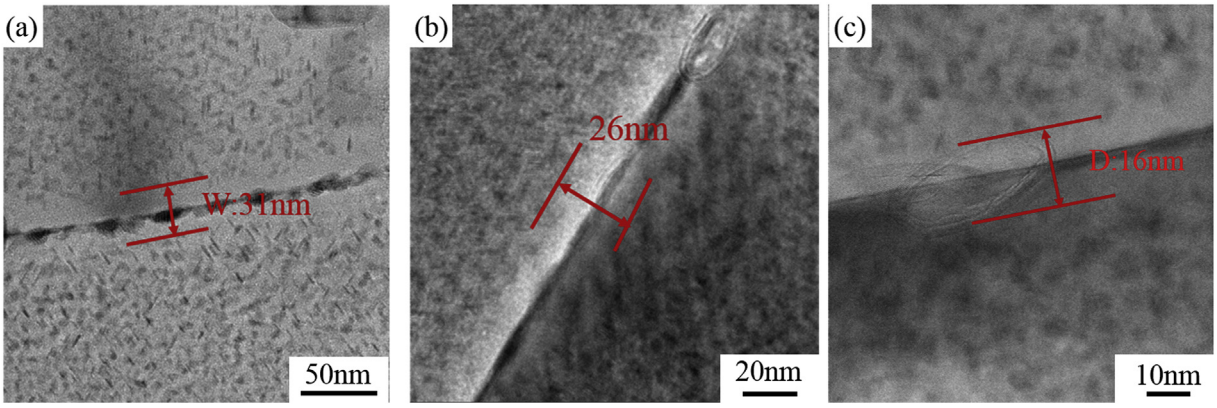

Fig. 7. The bright-field TEM micrographs of (a) composite A; (b) composite B; (c) composite C aged for 24 h showing the width of precipitate free zones.

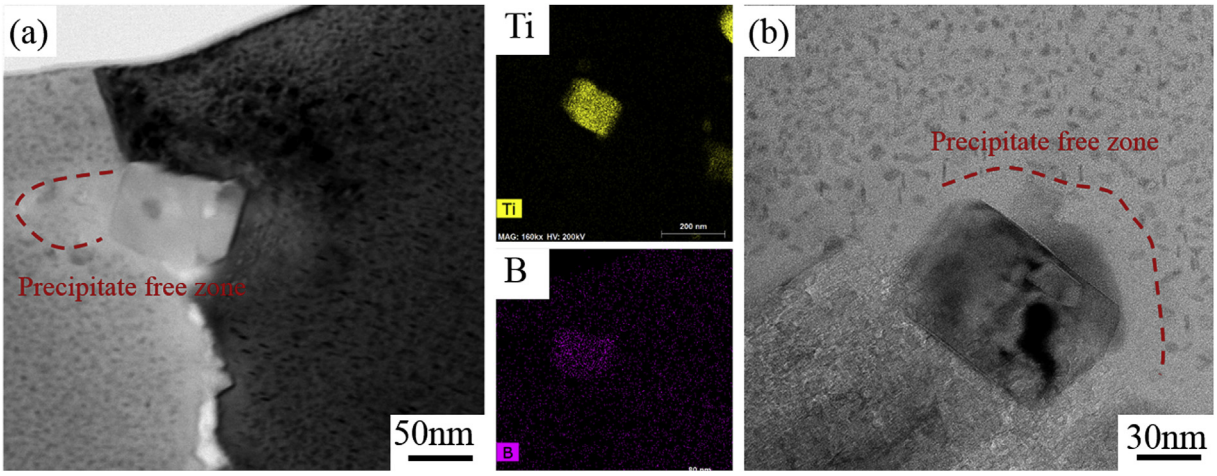

Fig. 8. Representative bright-field TEM images of the PFZs around the TiB_2 particles (a) located at the grain boundary; (b) within grains.

composites C, the hardness rapidly reaches the value of 236 HV and the hardness will basically not increase with proceeding aging. After aging for 6 h for composites A and B, the hardness reaches to 205.4 HV and 218.5 HV respectively. The composites A and B reach their peak hardness 219.2 HV and 228.7 HV after aging for 24 h. However, it is observed that the aging hardening response is more rapid for composites B than composites A at the initial stage of aging. Therefore, the introduction of more solute content not only increases the peak hardness of the composites but also accelerates hardening rate to peak hardness.

The typical room temperature engineering stress-strain curves of three composites aged for 24 h are illustrated in Fig. 10a and the mechanical properties are listed in Table 2. It can be seen that with increasing Zn content from 6.28 wt % to 8.32 wt %, the yield

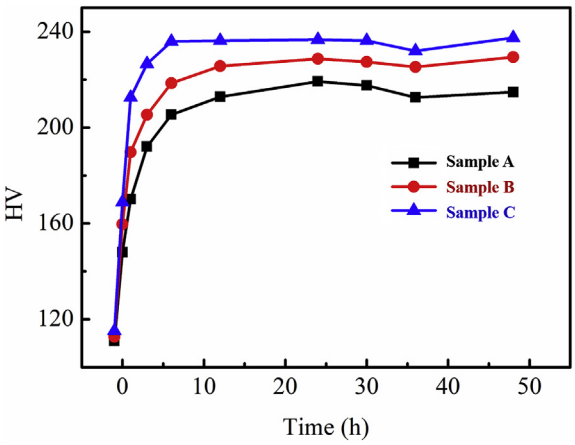

Fig. 9. The aging hardness response curves of composite A, B, C.

strength increase from 617 MPa to 693 MPa and ultimate strength increase from 691 MPa to 740 MPa, whereas the elongation decreases from 7.3% to 5.7%. However, with increasing Zn content from 8.32 wt % to 10.93 wt %, the yield strength just increases by 7 MPa and the elongation decreases from 5.7% to 2.3%. It may be due to the overage of composites C and more introduced impurities. In fact, the composites C reaches its peak hardening after aged for 6 h. B. F. Schultz et al. also prepared Al–Zn–Mg–Cu alloys with high Zn content to 12 wt % by squeeze casting and concluded that samples reached to its maximum hardness after artificial aging at 120 °C for approximately 6 h [44]. After the peak hardening, the precipitates will coarsen with proceeding artificial aging, which gives rise to a strength reduction. This tendency is similar to the report [27] where the yield strength does not increase with increasing the Zn from 10 wt % to 11 wt %. Furthermore, Table 2 also provides the strain-hardening exponent of each true stress-strain curve (calculated by engineering stress-strain curve) described by the simplest and more frequently used Hollomon equation as [45]:

$$\sigma = K\varepsilon_P^n \quad (1)$$

where σ is the true flow stress, ε_P is the plastic strain, K is the strength coefficient, and n is the strain-hardening exponent. It is observed that the strain-hardening exponent decreases with increasing Zn content. Fig. 10b shows the work hardening rate of each composite vs. plastic stress. At the initiation of plastic deformation, all the composites have a very high work hardening rate and the initial work hardening rate increases with increasing Zn content. With proceeding plastic deformation, the work hardening rate decays significantly. The work hardening rate of composite C decays most significantly and the absolute slope of composite C is highest. Finally, the work hardening rate of the composites decreases with increasing Zn content.

Table 2
The properties of the three aged composites.

Sample	$\sigma_{0.2}$ (MPa)	σ_b (MPa)	At (%)	E (GPa)	ρ (g/cm^3)	n
A	617 ± 2	691 ± 3	7.3 ± 08	82 ± 1	2.92 ± 0.14	0.084
B	693 ± 3	740 ± 6	5.7 ± 0.7	82 ± 1	2.89 ± 0.11	0.071
C	700 ± 3	739 ± 8	2.3 ± 0.6	83 ± 2	2.94 ± 0.12	0.043

4. Discussion

4.1. Size class model

In the present work, the size class model is undertaken to model the precipitation kinetics and predict the microstructure state-parameters including the precipitate size, number density, volume fraction, hardness and yield strength as a function of the aging time. The detailed description of the size class model is provided in the supplemental file.

The modeling is coded into a program on the computer and the modeling results are shown in Fig. 11 and Fig. 12. Fig. 11 shows the modeling precipitates number density, radius and volume fraction evolution as a function of aging time at 120 °C. It is observed that at the beginning of aging, the number density of the precipitates rapidly increases nearly linearly and then gradually tends to a plateau. With increasing the concentration of the solute elements, the slope of number density is steeper which indicates the accelerated precipitates nucleation rate and the transition of from linear dependency on aging time to the gradual plateau is advanced as indicated by the dotted line in Fig. 11a. And the number density of the precipitates is higher with increasing solute concentration. The variation of the volume fraction of precipitates during precipitation is similar to the variation of the number density. The accelerated increasing volume fraction is more obvious with increasing the solute concentration. The predicted volume fraction of precipitates aged for 24 h is 3.25%, 4.89%, and 6.49% respectively. Fig. 11c shows the precipitation radius evolution during the aging process. It could be observed that more addition of solute concentration accelerates the growth rate, which is similar to the variation of the number density and volume fraction. According to growth rate equation, the growth rate is proportional to the solute concentration in the matrix. However, the growth rate decelerates with continuous solute

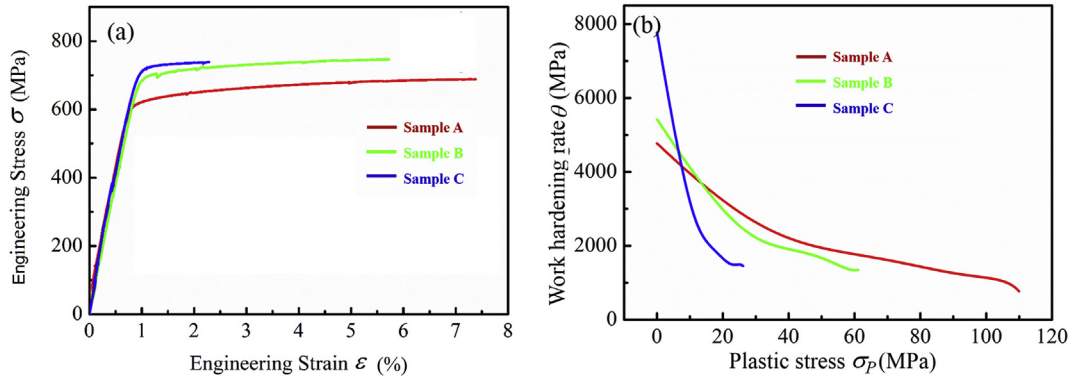

Fig. 10. (a) The typical engineering stress-strain curves of the composites fabricated in the present work; (b) the work hardening rate θ vs. plastic stress σ_P.

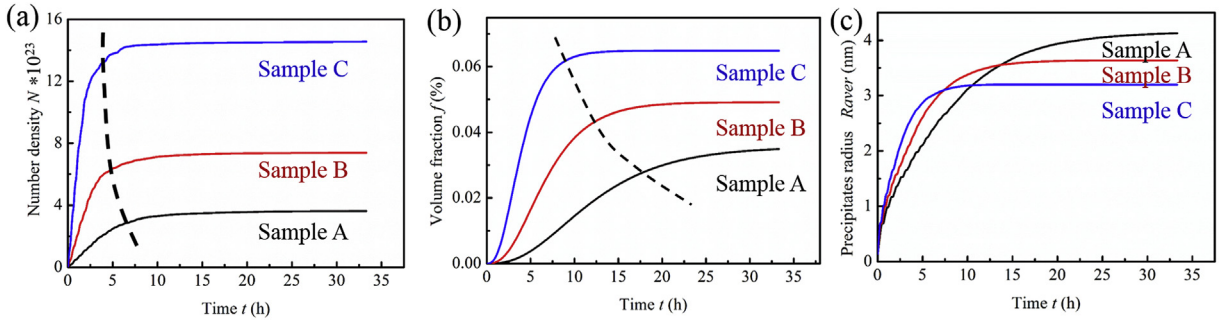

Fig. 11. The predicted (a) number density; (b) volume fraction; (c) precipitate radius as a function of aging time.

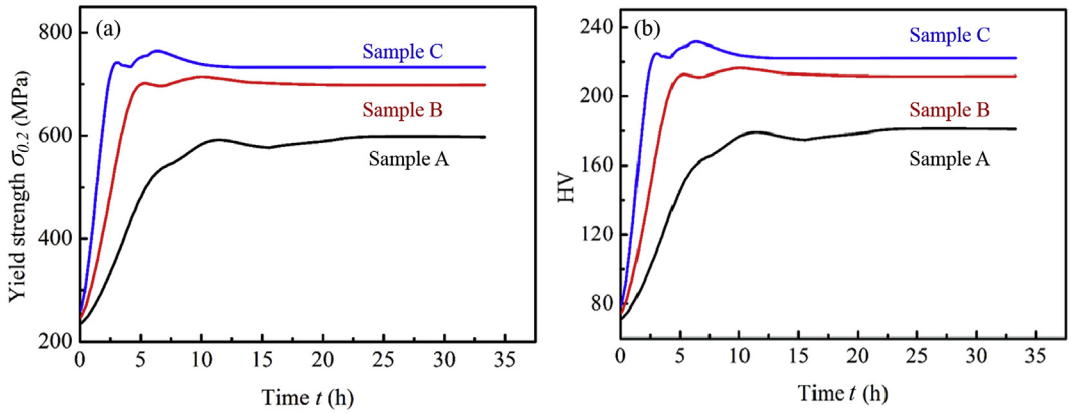

Fig. 12. The predicted (a) yield strength and (b) hardness during the precipitation process.

loss during precipitation. This decelerated effect is more obvious with increasing solute concentration due to the larger number density of precipitates. After a certain extent, the precipitation radius of sample B is larger that of sample C. Eventually, the precipitation radius is decreased with increasing solute concentration. The average predicted precipitate radius for samples A, B and C aging for 24 h is 4.04, 3.63 and 3.20 nm respectively, all of which is larger than the measured precipitate radius 3.12, 2.79 and 2.6 nm. This overestimation probably results from a limited measured number of precipitates from 10^{23} number density precipitates per volume fraction.

The predicted yield strength and hardness of the composites are shown in Fig. 12a and (b) respectively. The predicted yield strength of the composites aged for 24 h is 607, 708 and 743 MPa, while the measured yield strength is 613, 693 and 700 MPa respectively. The model predicts well the yield strength for sample A and B, while the model overestimates the yield strength for composite C. The model is based on the assumption that the solute elements are completely dissolved into the matrix and the precipitates would not form before aging treatment. However, in the practical case, the precipitates will nucleate instantaneously after solution treatment. Therefore, the predicted hardness is lower than the experimental hardness at the initial stage of aging. The addition of more solute concentration accelerates the aging hardness response as experiments observed in Fig. 9. This effect is correlated to the accelerated nucleation and growth rate with increasing solute concentration. In the model, the precipitates have a size distribution. Therefore, the precipitates strengthening contribution is calculated by summation of all size class rather than average precipitation radius, which is more reasonable.

4.2. The influence of the TiB_2 particles on the precipitation kinetics

The influence of TiB_2 particles on the precipitation kinetics can be viewed from dissolution and precipitation kinetics parameters. It is concluded from the precipitation kinetics model that the initial solute concentration has a significant effect on the precipitates size and volume fraction. Generally, the initial solute concentration C_0 is considered as a designed composition. Before aging, the composites are quenched in order to maximize the solute concentration in the matrix. For alloys, most of the interphases are dissolved into the matrix. For composites, it is observed that although most of the interphases are dissolved into the matrix, there are also interphases surrounded by TiB_2 particles clusters, which can't be dissolved into matrix completely. Geng et al. [22] have proposed that the introduction of particles lowers the contact surface area between interphases with the matrix. Therefore, the introduction of TiB_2 particles will make C_0 lower than the designed composition. However, in the present work, it is hard to quantify the specific solute concentration. In the present work, the deviation from the designed composition dependents on the distribution of the particles. Although the distribution of particles is generally uniform and the decrease of initial composition is low, there are also some particles clusters in the local region which would prevent the dissolution of interphases. Additionally, this effect is more severe with increasing solute concentration. Therefore, the predicted yield strength by the size class model is larger than the experimental values and this effect is more obvious with increasing Zn content.

The effect of the particles on the precipitation kinetics is complex. On the one hand, there are many studies which have reported that although the particle did not alter the precipitation sequence but accelerated precipitation kinetics [46,47]. This behavior is

generally attributed to enhanced nucleation/growth rate due to geometrically necessary dislocations (GNDs) around the particles. The dislocations around the particles are formed by quenching due to different coefficient of thermal expansion (CET). The density of GNDs can be estimated by the following expression [48]:

$$\rho_G = \frac{12V_p \Delta CTE \Delta T}{(1-V_p)bD} \tag{2}$$

where V_p is the volume fraction of the ceramic particles, ΔCET is the difference of CET between the particles and matrix, D is the particle size. In the present work, the introduced TiB_2 particles are in nanoscale, typically in the range of 25–500 nm [31]. If the average particle size is taken as 200 nm, the GNDs density due to quenching from 475 °C to room temperature can be estimated as 8.23×10^{13}. The physical properties of the aluminum matrix and TiB_2 particles are provided in Ref. [48]. These dislocations are assumed to distribute in the matrix plastic deformation zones (MPDZs). Dunand et al. have deduced the size of the MPDZs induced by the thermal mismatch in the silver chloride containing alumina fibers as [49]:

$$C_c = D\left(\frac{4 \cdot \Delta CET \cdot \Delta T \cdot E}{(5-4\nu)\sigma_y}\right)^{1/2} \tag{3}$$

where E, ν and σ_y are Young's modulus, Poisson ratio and yield strength of the matrix respectively. In the present work, the size of the MPDZs can be estimated about $0.87D$. It is supposed that there are larger precipitates in the MPDZs due to enhanced solute diffusion capability after aging. Instead, the larger precipitates are not found adjacent to the TiB_2 particles and PFZs with variable width distribution based on the shape of the TiB_2 particles are observed experimentally (Fig. 8). In fact, the models to predict the density of GNDs and size of MPDZs [48–50] due to thermal mismatch are based on the assumption that the mismatch strain α is beyond elastic limit and the prismatic dislocation loops can punch out from the matrix-interface to into the matrix. It is obvious from the equation that the size of the MPDZs depends on the yield strength of the matrix. It is concluded that the size of the MPDZs decreases with increasing the yield strength. The thermal mismatch α can be evaluated by the following expression:

$$\alpha = \Delta CET \cdot \Delta T \tag{4}$$

In Ref. [49], the thermal mismatch α reaches 2.1×10^{-4} with $\Delta T = 100$ K for the silver chloride containing alumina fibers, and for simplicity the stress equaling to the multiplication between the mismatch strain and Young's modulus reaches 10.92 MPa beyond the yield strength 1 MPa of purity silver chloride. In Ref. [50], the thermal mismatch α reaches 0.01 if the SiC_p/Al composites are quenched from 530 °C to room temperature, and the stress equaling to multiplication between the mismatch strain and Young's modulus reaches 698 MPa. Therefore, the Al matrix has been yielded. In these conditions, the prismatic dislocations are observed experimentally. In Ref. [43], the maximum thermal residual stress around the primary particle was estimated as 464 MPa by finite element simulation lower than the yield strength of the 725 alloys. The GNDs and larger precipitates are not found around the primary particles. In the present work, the thermal mismatch strain α reaches 0.0073 when the composites are quenched from 475 °C to room temperature, and the maximum stress obtained by multiplication between thermal mismatch α and Young's modulus is 503 MPa, which may be not higher enough to produce punch-out dislocations in the present work. However, the distribution of elastic strain energy around the TiB_2 particles give rise to different width of PFZs according to the shape of TiB_2 particles, which is similar to the distribution of γ'' around the primary carbide. In the present work, the modeling parameters about the diffusion constants of solute elements are not changed due to the introduction of nano-TiB_2 particles.

4.3. The influence of the Zn content on the work hardening rate

The Taylor equation is the basis of all the constitutive equation to describe the true stress-strain curve after plastic deformation which links the total dislocation density as:

$$\sigma_P = \alpha MGb\sqrt{\rho} \tag{5}$$

For pure metals, the original Kocks-Mecking model has been successfully used to model the dislocation density with plastic deformation as [51]:

$$\frac{d\rho}{d\varepsilon_p} = k_1\sqrt{\rho} - k_2\rho \tag{6}$$

where the first term represents the dislocation storage capacity such as multiplication of mobile dislocations, the second term represents the dislocation recovery including cross-slip mechanism at low temperature and dislocation climb at elevated temperature. Combined equation (20) and (21), the plastic stress dependency of the work hardening rate can be derived in the form of:

$$\theta = \theta_0 - \frac{\theta_0}{\sigma_S}\sigma_P = \theta_0 - B\sigma_P \tag{7}$$

where $\theta_0 = \alpha Gbk_1/2$, and $B = k_2M/2$. It indicates the linear dependence of the work hardening rate on the plastic stress for the pure metals. For pure aluminum, the y-axis intercept is assumed to equal to $G/20$. In the present work, it is obvious that the initial work hardening rate which is the intercept with y-axis when plastic stress is zero is higher than pure aluminum and increases with increasing Zn content. The increased work hardening rate is resulted from a large amount of precipitates and TiB_2 particles in the composites. The simultaneous deformation of a large amount of precipitates and TiB_2 particles with different elastic modulus will lead to the formation of geometrically necessary dislocations [52,53]. In addition, the development of the internal stress due to non-shearable particles such as larger precipitates and TiB_2 particles contributes to the enhanced work hardening rate [54,55]. Modified KM model was developed which took the additional storage of geometrically necessary dislocations into consideration as [56]:

$$\frac{d\rho}{d\varepsilon_P} = k_1\sqrt{\rho} - k_2\rho + \frac{1}{bl} \tag{8}$$

The additional dislocation storage due to second phases including precipitates and TiB_2 particles is inverse proportional to particle spacing l. Combined equation (20) with (23), the modified dependency of work hardening rate can be derived as:

$$\theta = \theta_0 + \frac{\alpha GM}{2l\sqrt{\rho}} - B\sigma_P = \theta_0^{'} - B\sigma_P \tag{9}$$

The particle spacing decreases with increasing Zn content, thus the initial work hardening rate $\theta_0^{'}$ is larger with increasing Zn content.

The influence of the Zn content on the dislocation recovery rate can be viewed in terms of critical annihilation distance, i.e. $k_2 = 2y/b$. The stress field of around the second phases including precipitates and TiB_2 particles favours the cross-slip of mobile

dislocations [55]. Simar et al. [56] have deduced a relation to describe the rate of dislocation dynamic recovery which took the additional dislocations annihilation in pairs due to the introduction of second phases into consideration in the form as:

$$k_2 = k_2^0 exp\left(-\frac{l_0}{l}\right) + k_2^p\left[1 - exp\left(-\frac{l_0}{l}\right)\right] \quad (10)$$

where the first term represents the rate of dislocation recovery without second phases, the second term shows the rate of dislocation recovery with second phases, l_0 is the mean moving dislocation distance. And $k_2^p \gg k_2^0$, so the above expression can be modified to:

$$k_2 \approx k_2^p\left[1 - exp\left(-\frac{l_0}{l}\right)\right] \quad (11)$$

It is obvious that the k_2 increase with decreasing the particle spacing. Therefore, in the present work, the particle spacing decreases with increasing Zn content, thus the dislocation recovery rate will increase with more addition of Zn content as experiment observed.

5. Conclusions

In the present work, the microstructure and precipitation kinetics of the TiB_2/Al−Zn−Mg−Cu composites with different Zn content fabricated by powder metallurgy were studied. And the size class model extended by the KWN model was used to model the precipitates evolution during aging. The following conclusions can be derived:

1. The addition of more Zn content increases the faction of formed interphases during extrusion and does not change the precipitation types after aging.
2. The formed interphases during extrusion are preferentially nucleated at the facet of the TiB_2 particles and the TiB_2 particles clusters prevent the dissolution of the interphases.
3. The size class model predicts well the precipitate size and volume fraction depending on aging time.
4. The accelerated aging hardening response is observed for composites with more Zn content, which is attributed to the accelerated precipitation nucleation rates due to higher chemical potential.
5. The precipitate free zones form around the TiB_2 particles after aging treatment and the larger precipitates adjacent to the matrix-particle interface are not found.
6. The increased initial work hardening rate and the dislocation recovery rate are observed with more Zn addition which is resulted from the larger fraction of precipitates and narrower precipitates spacing.

Declaration of competing interest

No potential conflict of interest was reported by the authors.

Acknowledgment

This work is financially supported by the National Key Research and Development Program of China (Grant No. 2016YFB1100103); the National Natural Science Foundation of China (Grant No. 51971137 and No. 11875192); the Conseil Regional du Nord-Pas de Calais and the European Regional Development Fund; Many thanks are due to the faculty of TESCAN China for their help on SEM and EBSD.

Appendix A. Supplementary data

Supplementary data to this article can be found online at https://doi.org/10.1016/j.jallcom.2019.152584.

References

[1] H.C. Li, F.Y. Gao, S. Guo, Z.L. Ning, Z.Y. Liu, Y.D. Jia, S. Scudino, T. Gemming, J.F. Sun, Microstructures and properties evolution of spray-deposited Al-Zn-Mg-Cu-Zr alloys with scandium addition, J. Alloy. Comp. 691 (2017) 482−488.
[2] K.K. Ma, H.M. Wen, T. Hu, T.D. Topping, D. Ishiem, D.N. Seidman, E.J. Lavernia, J.M. Schoenung, Mechanical behavior and strengthening mechanisms in ultrafine grain precipitation-strengthened aluminum alloy, Acta Mater. 62 (2014) 141−155.
[3] Y.F. Song, X.F. Ding, L.R. Xiao, X.J. Zhao, Z.Y. Cai, L. Guo, Y.W. Li, Z.Z. Zhang, Effects of two-stage aging on the dimensional stability of Al-Cu-Mg alloy, J. Alloy. Comp. 701 (2017) 508−514.
[4] Y. Chen, N. Gao, G. Sha, S.P. Ringer, M.J. Starink, Microstructural evolution, strengthening and thermal stability of an ultrafine −grained Al-Cu-Mg alloy, Acta Mater. 109 (2016) 202−212.
[5] W. Chrominski, M. Lewandowska, Precipitation phenomena in ultrafine grained Al-Mg-Si alloy with heterogeneous microstructure, Acta Mater. 103 (2016) 547−557.
[6] Y.X. Lai, B.C. Jiang, C.H. Liu, Z.K. Chen, C.L. Wu, J.H. Chen, Low-alloy-correlated reversal of the precipitation sequence in Al-Mg-Si alloys, J. Alloy. Comp. 701 (2017) 94−98.
[7] B. Li, Q.L. Pan, C.P. Chen, H.H. Wu, Z.M. Yin, Effects of solution treatment on microstructural and mechanical properties of Al-Zn-Mg alloy by microalloying with Sc and Zr, J. Alloy. Comp. 664 (2016) 553−564.
[8] Y. Liu, D.M. Jiang, W.L. Xie, J. Hu, B. Ma, Solidification phases and their evolution during homogenization of a DC cast Al-8.35Zn-2.5Mg-2.25Cu alloy, Mater. Char. 93 (2014) 173−183.
[9] D. Xu, Z.H. Li, G.J. Wang, X.W. Li, X.Y. Lv, Y.A. Zhang, Y.Q. Fan, Phase transformation and microstructure evolution of an ultra-high strength Al-Zn-Mg-Cu alloy during homogenization, Mater. Char. 131 (2017) 285−297.
[10] G. Sha, A. Cerezo, Early-stage precipitation in Al-Zn-Mg-Cu alloy (7050), Acta Mater. 52 (2004) 4503−4516.
[11] M. Dumont, W. Lefebvre, B. Doisneau-Cottignies, A. Deschamps, Characterization of the composition and volume fraction of η′ and η precipitates in an Al-Zn-Mg alloy by a combination of atom probe, small-angle X-ray scattering and transmission electron microscopy, Acta Mater. 53 (2005) 2881−2892.
[12] J.C. Werenskiold, A. Deschamps, Y. Brechet, Characterization and modeling of precipitation kinetics in an Al-Zn-Mg alloy, Mater. Sci. Eng. A 293 (2000) 267−274.
[13] J. Taendl, A. Orthacker, H. Amenitsch, G. Kothleitner, C. Poletti, Influence of the degree of scandium supersaturation on the precipitation kinetics of rapidly solidified Al-Mg-Sc-Zr alloys, Acta Mater. 117 (2016) 43−50.
[14] A. Deschamps, Y. Brechet, Influence of predeformation and aging of an Al-Zn-Mg alloy—II. Modeling of precipitation kinetics and yield stress, Acta Mater. 47 (1999) 293−305.
[15] M. Perez, M. Dumont, D. Acevedo-Reyes, Implementation of classical nucleation and growth theories for precipitation, Acta Mater. 56 (2008) 2119−2132.
[16] J.D. Robson, M.J. Jones, P.B. Prangnell, Extension of the N-model to predict competing homogeneous and heterogeneous precipitation in Al-Sc alloys, Acta Mater. 51 (2003) 1453−1468.
[17] C.D. Wu, K.K. Ma, D.L. Zhang, J.L. Wu, S.Y. Xiong, G.Q. Luo, J. Zhang, F. Chen, Q. Shen, L.M. Zhang, E.J. Lavernia, Precipitation phenomena in Al-Zn-Mg alloy matrix composites reinforced with B_4C particles, Sci. Rep. (2017) 1−11.
[18] A. Mandal, B.S. Murty, Effect of TiB_2 particles on aging response of Al-4Cu alloy, Mater. Sci. Eng. A 386 (2004) 296−300.
[19] Y. Cui, T.Z. Jin, L.G. Cao, F.B. Liu, Aging behavior of high volume fraction SiCp/Al composites fabricated by pressureless infiltration, J. Alloy. Comp. 681 (2016) 233−239.
[20] Z. Chen, J. Li, A. Borbely, G. Ji, S.Y. Zhong, Y. Wu, M.L. Wang, H.W. Wang, The effects of nanosized particles on microstructural evolution of an in-situ TiB_2/6063Al composite produced by friction stir processing, Mater. Des. 88 (2015) 999−1007.
[21] M. Wang, Y. Wang, J. Liu, Z. Chen, H. Chen, Y. Wu, F.G. Zhang, H.W. Wang, Effects of Zn content on microstructures and mechanical properties of in-situ TiB_2/Al-Zn-Mg-Cu composites subjected to hot extrusion, Mater. Sci. Eng. A 742 (2019) 364−372.
[22] J.W. Geng, T.R. Tian, Y. Ma, M.L. Wang, The solution treatment of in-situ submicron TiB_2/2024 Al composites, Mater. Des. 98 (2016) 186−193.
[23] Q. Yang, Y.T. Liu, J. Liu, L. Wang, Z. Chen, M.L. Wang, S.Y. Zhong, Y. Wu, H.W. Wang, Microstructure evolution of the rapidly solidified alloy powders and composite powders, Mater. Des. 182 (2019) 1−12.
[24] M.A. Jabbari Taleghani, E.M. Ruiz Navas, J.M. Torralba, Microstructural and mechanical characterization of 7075 aluminum alloy consolidated from a premixed powder by cold compaction and hot extrusion, Mater. Des. 55 (2014) 674−682.
[25] P.C. Bai, X.H. Hou, X.Y. Zhang, C.W. Zhao, Y.M. Xing, Microstructure and mechanical properties of a large billet of spray formed Al-Zn-Mg-Cu alloy with

high Zn content, Mater. Sci. Eng. A 508 (2009) 23–27.
[26] M. Wang, Y. Wang, J. Liu, Z. Chen, H. Chen, Y. Wu, F.G. Zhang, H.W. Wang, Effects of Zn content on microstructures and mechanical properties of in-situ TiB2/Al-Zn-Mg-Cu composites subjected to hot extrusion, Mater. Sci. Eng. A 742 (2019) 364–372.
[27] Z.Y. Chen, Y.K. Mo, Z.R. Nie, Effect of Zn content on the microstructure of super-high strength Al-Zn-Mg-Cu alloys, Metall. Mater. Trans. A 44 (2013) 3910–3920.
[28] Y.L. Deng, L. Wan, Y.Y. Zhang, X.M. Zhang, Influence of Mg content on quench sensitivity of Al-Zn-Mg-Cu alloys, J. Alloy. Comp. 509 (2011) 4636–4642.
[29] Z. Chen, J. Li, A. Borbely, G. Ji, S.Y. Zhong, Y. Wu, M.L. Wang, H.W. Wang, The effects of nanosized particles on microstructural evolution of an in-situ TiB_2/6063Al composite produced by friction stir processing, Mater. Des. 88 (2015) 999–1007.
[30] B.L. Silva, J.G. Dessi, L.F. Gomers, M.M. Peres, M.V. Cante, J.E. Spinelli, Assessing microstructures and mechanical resistances of as-atomized and as-extruded samples of Al-1wt%Fe-1wt%Ni alloy, J. Alloy. Comp. 691 (2017).
[31] Y. Tang, Z. Chen, A. Borbely, G. Ji, S.Y. Zhong, D. Schryvers, V. Ji, H.W. Wang, Quantitative study of particle size distribution in an in-situ grown Al–TiB_2 composite by synchrotron X-ray diffraction and electron microscopy, Mater. Char. 102 (2015) 131–136.
[32] H. Liang, S.L. Chen, Y. A, A thermodynamic description of the Al-Mg-Zn system, Metall. Mater. Trans. A (1997) 1725–1734.
[33] M.J. Styles, C.R. Hutchinson, Y. Chen, A. Deschamps, T.J. Bastow, The coexistence of two S (Al2CuMg) phase in Al-Cu-Mg alloys, Acta Mater. 60 (2012) 6940–6951.
[34] S.K. Maloney, K. Hono, I.J. Polmear, S.P. Ringer, The chemistry of precipitates in an aged Al-2.1Zn-1.7Mg at. % alloy, Scr. Mater. 41 (1999) 1031–1038.
[35] J.Z. Liu, J.H. Chen, X.B. Yang, S. Ren, C.L. Wu, H.Y. Xu, J. Zou, Revisiting the precipitation sequence in Al-Zn-Mg-based alloys by high-resolution transmission electron microscopy, Scr. Mater. 63 (2010) 1061–1064.
[36] H.M. Wang, Y.P. Yi, S.Q. Huang, Influence of pre-deformation and subsequent ageing on the hardening behavior and microstructure of 2219 aluminum alloy forgings, J. Alloy. Comp. 685 (2016) 941–948.
[37] T. Ogura, S. Hirosawa, A. Cerezo, T. Sato, Atom probe tomography of nanoscale microstructure within precipitate free zones in Al-Zn-Mg-(Ag) alloys, Acta Mater. 58 (2010) 5714–5723.
[38] G.W. Lorimer, R.B. Nicholson, Further results on the nucleation of precipitates in the Al-Zn-Mg system, Acta Metall. 14 (1966) 1009–1013.
[39] J.D. Embury, R.B. Nicholson, The nucleation of precipitates: the system Al-Zn-Mg, Acta Metall. 13 (1965) 403–417.
[40] M. Raghavan, Microstructure of precipitate free zones (PFZ) in Al-Zn-Mg and Cu-Ni-Nb alloys, Metall. Mater. Trans. A 11 (1980) 993–999.
[41] Y.Q. Chen, S.P. Pan, S.W. Tang, W.H. Liu, C.P. Tang, F.Y. Xu, Formation mechanisms and evolution of precipitate-free zones at grain boundaries in an Al-Cu-Mg-Mn alloy during homogenization, J. Mater. Sci. 51 (2016) 7780–7792.
[42] T. Sanders, E. Ludwiczak, R. Sawtell, The fracture behavior of recrystallized Al-2.8%Li-0.3% Mn sheet, Mater. Sci. Eng. A 43 (1980) 247–260.
[43] M. Song, J.F. Wen, Z. Jiao, G.S. Was, Elastic strain energy control of precipitate free zone around primary carbides in nickel base alloy, Acta Mater. 120 (2016) 138–149.
[44] J.B. Ferguson, B.F. Schultz, J.C. Mantas, H. Shokouhi, P.K. Rohatgi, Effect of Cu, Zn, and Mg concentration on heat treating behavior of squeeze cast Al-(10-12) Zn-(3.0-2.4Mg)-(0.8-1)Cu, Metals 4 (2014) 314–321.
[45] G. Angella, F. Zanardi, R. Donnini, On the significance to use dislocation-density-related constitutive equations to correlate strain hardening with microstructure of metallic alloys: the case of conventional and austempered ductile irons, J. Alloy. Comp. 669 (2016) 262–271.
[46] I. Dutta, C.P. Harper, G. Dutta, Role of Al_2O_3 particulate reinforcements on precipitation in 2014 Al matrix composites, Metall. Mater. Trans. A 25 (1994) 1591–1602.
[47] I. Dutta, S.M. Allen, J.L. Hafley, Effect of reinforcement on the aging response of cast 6061 Al- Al_2O_3 particulate composites, Mater. Trans. 22 (1991) 2553–2563.
[48] M.L. Wang, D. Chen, Z. Chen, Y. Wu, F.F. Wang, N.H. Ma, H.W. Wang, Mechanical properties of in-situ TiB_2/A356 composites, Mater. Sci. Eng. A 590 (2014) 246–254.
[49] D.C. Dunand, A. Mortensen, On plastic relaxation of thermal stresses in reinforced metals, Acta Metall. Mater. 39 (1991) 127–139.
[50] M. Taya, K.E. Lulay, D.J. Lloyd, Strengthening of a particulate metal matrix composites by quenching, Acta Metall. Mater. 39 (1991) 73–87.
[51] Y. Estrin, H. Mecking, A unified phenomenological description of work hardening rate and creep based on one-parameter models, Acta Metall. 32 (1984) 57–70.
[52] M.F. Ashby, The deformation of plastically non-homogeneous materials, Philos. Mag. (1969) 399–422.
[53] F. Fazeli, W.J. Poole, C.W. Sinclair, Modeling the effect of Al3Sc precipitates on the yield stress and work hardening of Al-Mg-Sc alloy, Acta Mater. 58 (2008) 1909–1918.
[54] G. Fribourg, Y. Brechet, A. Deschamps, A. Simar, Microstructure-based modelling of isotropic and kinetics strain-hardening in a precipitation-hardened aluminum alloy, Acta Mater. 59 (2011) 3621–3635.
[55] H. Proudhon, W.J. Poole, X. Wang, Y. Brechet, The role of internal stresses on the plastic deformation of the Al-Mg-Si alloy AA6111, Philos. Mag. 88 (2008) 621–640.
[56] A. Simar, Y. Brechet, B. de Meester, A. Denquin, T. Pardoen, Sequential modeling of local precipitation, strength and strain hardening in friction stir welds of aluminum alloy 6005A-76, Acta Mater. 55 (2007) 6133–6143.